Accelerating self-imaging effect for Airy pulse trains

Tianwen Han,[1] Bing Wang,[1,*] and Peixiang Lu[1,2,†]

[1]*Wuhan National Laboratory for Optoelectronics and School of Physics,*
Huazhong University of Science and Technology, Wuhan 430074, China
[2]*Laboratory for Optical Information Technology, Wuhan Institute of Technology, Wuhan 430205, China*

We investigate the temporal accelerating self-imaging effect for a train of Airy pulses propagating in optical fibers. The group velocity of the Airy pulses is varying during propagation, resulting in a parabolic time-space trajectory of self-imaging. The acceleration is determined by the main-lobe width of the Airy pulses. Meanwhile, the self-imaging distance depends both on the main-lobe width and the time interval of the pulses. In addition, the trajectory of self-imaging can be modified by imposing a linearly varying phase on the input pulse train. By applying third-order dispersion, we also realize the temporally magnified self-imaging of the Airy pulse trains. As the Airy pulses possess infinite energy, the self-imaging can be observed for infinite times. If the pulses are truncated to have finite-energy, the self-imaging maintains only in a limited distance. The study provides a promising way to control the self-imaging of optical pulses and may find applications in optical communication and signal processing systems.

I. INTRODUCTION

Talbot effect refers to the self-imaging of a periodic optical field, which was first discovered by Talbot in 1836 [1]. The effect has been studied in a variety of physical fields, such as matter waves [2], plasmonics [3], and metamaterials [4]. The discrete Talbot effect has also been observed in waveguide arrays and manifests different features from continuous mediums [5–7]. So far, the effect has found many applications in nonlinear optics [8,9], quantum optics [10], and x-ray imaging [11]. Considering the time-space duality and the analogy between spatial Fresnel diffraction and temporal group velocity dispersion (GVD) [12], the Talbot effect has been extended to time domain by injecting periodic optical pulse trains into the optical fiber with GVD [13–17]. In the Talbot effects mentioned above, the incident field has to be periodic and is reproduced along the straightforward propagation direction [18–20].

Recently, the spatial Airy-Talbot effect has been theoretically proposed and experimentally demonstrated [21], where the incident field is composed by the superposition of many Airy beams [22,23] with a lateral deviation between each other. Each Airy beam has a profile of intensity in the form of an Airy function [24], which is a nonspreading solution of the linear Schrödinger equation and has many unique features of self-accelerating, diffraction-free, and self-healing [22,23,25–27]. Differing from the traditional Talbot effect, the Airy-Talbot effect shows self-imaging along a curved trajectory. On account of the time-space duality, the temporal Airy pulse [22,23] can be obtained by imparting a cubic phase modulation onto the Gaussian pulse [28]. Accordingly, the Airy pulses manifest features of free dispersion,

self-acceleration [29], and self-reconstruction when propagating in the fibers. The self-acceleration of Airy beams leads to a curved propagation trajectory in space. Comparably, the self-acceleration of Airy pulses conduces to a varying group velocity during propagation [29]. The linear and nonlinear propagation dynamics of Airy pulses have been extensively investigated [30–38] and found great applications in supercontinuum generation and signal processing [39,40].

In this work, we shall study the temporal Airy-Talbot effect of a train of Airy pulses propagating in optical fibers. We show that the self-imaging of the input wave train composed by the superposition of Airy pulses is accelerating during propagation. The acceleration is determined by the main-lobe width of the Airy pulses. The corresponding self-imaging distance can be manipulated by varying the time interval and the main-lobe width of the pulses. Unlike traditional Talbot effect, the incident field needs not be periodic in the Airy-Talbot effect. In addition, a linearly varying phase is also imposed on the input pulse train in order to control the trajectory of self-imaging. We further reveal the influence of third-order dispersion on the self-imaging positions. Given the practical Airy pulses with limited time duration, the self-imaging of incident wave trains composed of finite-energy Airy pulses are also investigated. The study may find the applications of optical field self-imaging for both optical communication and signal processing.

II. THEORETICAL MODEL

The evolution of an optical pulse in the dispersive optical fiber is governed by [12]

$$\frac{\partial A}{\partial z} + \frac{i}{2}\beta_2 \frac{\partial^2 A}{\partial \tau^2} - \frac{1}{6}\beta_3 \frac{\partial^3 A}{\partial \tau^3} = 0, \tag{1}$$

where $A(\tau, z)$ denotes the slowly varying envelope of the optical pulse. β_2 and β_3 stand for the GVD and the third-order

---

*wangbing@hust.edu.cn
†lupeixiang@hust.edu.cn

dispersion (TOD) coefficients of the fiber, respectively. The impact of the higher-order dispersion on pulse propagation is usually negligible with respect to that of GVD in the common single-mode fibers (SMFs). $\tau = t - z/v_{g0}$ is the retarded time in the frame of reference, which is moving at the initial pulse group velocity v_{g0}. The real time and propagation distance are denoted by t and z, respectively. The equation is valid when the incident field has weak intensity, and thus the nonlinear effects can be ignored. Here the loss of the fiber is not considered since only the field profile at a certain distance is mainly concerned. For an input field $A(\tau, 0)$ at $z = 0$, the evolution of the field is given by

$$A(\tau, z) = \frac{1}{2\pi} \int_{-\infty}^{+\infty} \tilde{A}(\omega, 0) \exp\left(i\frac{\beta_2 z}{2}\omega^2 + i\frac{\beta_3 z}{6}\omega^3\right) \exp(-i\omega\tau)d\omega, \tag{2}$$

where $\tilde{A}(\omega, 0)$ represents the Fourier transform of $A(\tau, 0)$.

We consider the propagation of a wave train comprised of a superposition of many Airy pulses with a constant time interval T

$$A(\tau, 0) = \sum_{n\in\mathbb{Z}} c_n \mathrm{Ai}\left(\frac{\tau}{t_0} - n\frac{T}{t_0}\right) \exp\left[a\left(\frac{\tau}{t_0} - n\frac{T}{t_0}\right)\right], \tag{3}$$

where $\mathrm{Ai}(\cdot)$ denotes the Airy function with a ($0 < a < 1$) being the truncation factor. c_n is a complex coefficient and contains information of amplitude and phase for each Airy pulse component. All the Airy pulses have the same main-lobe width t_0 [35]. Substituting Eq. (3) into Eq. (2), we obtain

$$A(\tau, z) = \frac{1}{\theta^{1/3}} \exp\left[-\frac{a\beta_2^2 z^2}{2\theta^2 t_0^4} + \frac{a^2 b(1 + ab)|\beta_2|z}{3\theta^2 t_0^2}\right] \exp\left[i\frac{|\beta_2|z}{2\theta^2 t_0^2}\left(a^2 + \frac{\tau}{t_0} - \frac{\beta_2^2 z^2}{6t_0^4}\right) + i\frac{b\beta_2^2 z^2}{2\theta^2 t_0^4}\left(a^2 - \frac{\tau}{t_0}\right)\right]$$

$$\times \sum_n c_n \mathrm{Ai}\left\{\frac{1}{\theta^{4/3}}\left[\left(\frac{\tau}{t_0} - n\frac{T}{t_0} - \frac{\beta_2^2 z^2}{4t_0^4} + ia\frac{|\beta_2|z}{t_0^2}\right) - b\frac{|\beta_2|z}{t_0^2}\left(\frac{\tau}{t_0} - n\frac{T}{t_0} - a^2\right)\right]\right\}, \tag{4}$$

$$\times \exp\left\{\frac{1}{\theta^2}\left[a\left(\frac{\tau}{t_0} - n\frac{T}{t_0}\right) + ab\frac{|\beta_2|z}{t_0^2}\left(\frac{\tau}{t_0} - n\frac{T}{t_0}\right)\right]\right\}$$

$$\times \exp\left[i\frac{1}{\theta^2}\left(-\frac{n|\beta_2|Tz}{2t_0^3} + \frac{bn\beta_2^2 z^2 T}{2t_0^5}\right)\right]$$

where $\theta = 1 + \mathrm{sgn}(\beta_2)\beta_3 z/2t_0^3$ and $b = -\beta_3/2\beta_2 t_0$. In the absence of higher-order dispersion, i.e., $\beta_3 = b = 0$ and $\theta = 1$, Eq. (4) simplifies to

$$A(\tau, z) = \sum_n c_n \mathrm{Ai}\left(\frac{\tau}{t_0} - n\frac{T}{t_0} - \frac{\beta_2^2 z^2}{4t_0^4} + ia\frac{|\beta_2|z}{t_0^2}\right) \exp\left[a\left(\frac{\tau}{t_0} - n\frac{T}{t_0} - \frac{\beta_2^2 z^2}{2t_0^4}\right)\right] \exp\left[i\frac{|\beta_2|z}{2t_0^2}\left(a^2 + \frac{\tau}{t_0} - \frac{\beta_2^2 z^2}{6t_0^4} - n\frac{T}{t_0}\right)\right], \tag{5}$$

and the corresponding intensity has the form

$$I(\tau, z) = \left|\sum_{n\in\mathbb{Z}} c_n \mathrm{Ai}\left(\frac{\tau}{t_0} - \frac{\beta_2^2 z^2}{4t_0^4} - n\frac{T}{t_0} + ia\frac{|\beta_2|}{t_0^2}z\right) \exp\left(-i\frac{|\beta_2|z}{2t_0^3}nT\right) \exp\left[a\left(\frac{\tau}{t_0} - n\frac{T}{t_0} - \frac{\beta_2^2}{2t_0^4}z^2\right)\right]\right|^2. \tag{6}$$

From Eq. (6), one can find that the initial intensity profile is reshaped during propagation owing to the interference of Airy pulses. However, as the propagation distance satisfies the condition $|\beta_2|Tz/2t_0^3 = 2m\pi$ with m being a nonzero integer, we have $\exp(-in|\beta_2|Tz/2t_0^3) = 1$. That is, all the Airy pulses are in-phase. Consequently, similar to the spatial Airy-Talbot effect, the input pulse train repeats itself periodically along the parabolic trajectory in the τ-z plane [35], which is given by

$$\tau = \frac{\beta_2^2}{4t_0^3}z^2 + nT. \tag{7}$$

The corresponding Newtonian equations describing the trajectory read [31]

$$\frac{d^2\tau}{dz^2} = \frac{\beta_2^2}{2t_0^3} = g,$$

$$\frac{d\tau}{dz} = \frac{\beta_2^2}{2t_0^3}z = v(z). \tag{8}$$

Here g plays the role of acceleration and $v(z)$ acts as a velocity. The schematic diagram of the temporal Airy-Talbot effect is shown in Fig. 1, and the Airy-Talbot distance is

$$z_T = \frac{4\pi t_0^3}{|\beta_2|T}. \tag{9}$$

It should be mentioned that the Airy-Talbot effect is independent of the complex coefficients c_n. In fact, from Eqs. (3)–(6), one sees that the coefficients c_n are arbitrarily chosen. Thus the accelerating self-imaging wave train needs not be periodic, which is contrary to the requirement of periodic incident field in traditional Talbot effects.
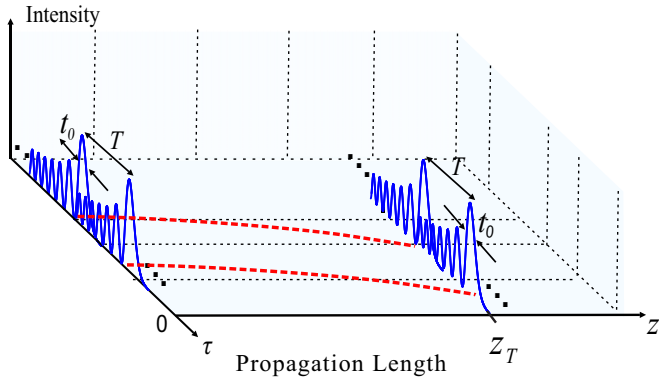
FIG. 1. Schematic diagram of the temporal Airy-Talbot effect.

III. RESULTS AND DISCUSSION

A. Airy-Talbot effect in the absence of TOD

To confirm the above theoretical analysis, we simulate the evolution of a train of Airy pulses in optical fibers by using the split-step Fourier transform method [12]. We shall first consider the case of ideal Airy pulses with $a = 0$ in the presence of GVD. The incident field is comprised of a superposition of 11 Airy pulses with the main-lobe width $t_0 = 10$ ps and a constant time interval $T = 83.33$ ps. The GVD is chosen as $\beta_2 = -20$ ps^2/km. From Eq. (9), one gets the Airy-Talbot distance $z_T = 7.54$ km. The temporal evolution of the pulse train in the $\tau - z$ plane is illustrated in Fig. 2(a). The wave train repeats itself periodically along parabolic time-space trajectories during propagation. The parabolic trajectory
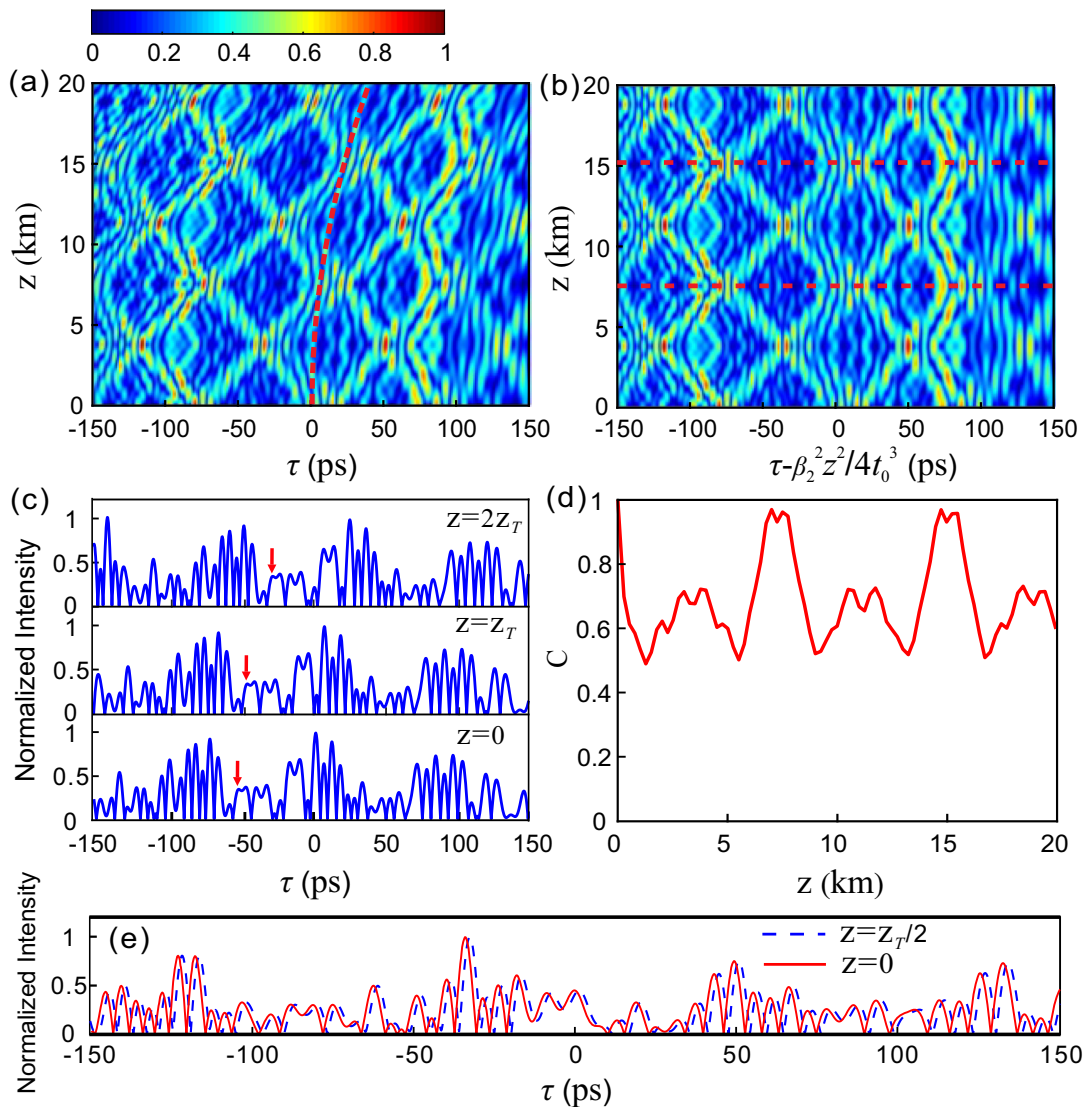

FIG. 2. (a) Temporal evolution of the Airy pulse train in the τ-z plane. The wave train is composed by 11 Airy pulses, each multiplied by a different random coefficient c_n. The self-imaging trajectory for $n = 0$ is marked by the red dashed curve. (b) Intensity carpet in the accelerating frame. The red dashed lines denote the first and second self-imaging locations. (c) Normalized intensity profiles at $z = 0$, z_T, and $2z_T$. (d) Cross-correlation coefficient vs the propagation distance in the accelerating coordinates. (e) Normalized intensity profile at $z_T/2$ (blue dashed curve), and the initial intensity envelope with the redefined coefficients $c_n' = (-1)^n c_n$ (red solid curve). Parameters are $t_0 = 10$ ps, $T = 83.33$ ps, and $c_n = [0.3371, 0.1622, 0.7943, 0.3312, 0.5285, 0.1656, 0.6020, 0.2650, 0.6541, 0.6892, 0.7482]$.
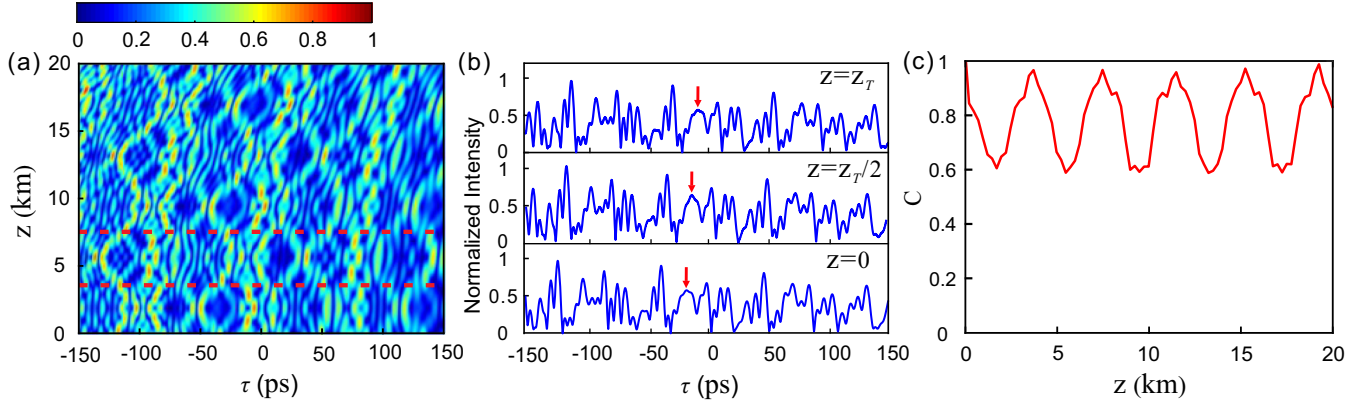
FIG. 3. (a) Temporal evolution of the Airy pulse train by choosing $c_n = 1$ if n is even and $c_n = i$ if n is odd. (b) Normalized intensity profiles at $z = 0$, $z_T/2$, and z_T, indicated by the red dashed lines in (a). (c) Cross-correlation coefficient vs the propagation distance in the accelerating coordinates. Other parameters are the same as in Fig. 2(a).

$\tau = z^2/10$ for $n = 0$ is plotted with the red dashed curve in Fig. 2(a). The corresponding intensity carpet in the accelerating frame is shown in Fig. 2(b), where the self-imaging effect can be visualized more clearly. The two red dashed lines in Fig. 2(b) represent the first and second self-imaging positions. Figure 2(c) shows the normalized intensity profiles at $z = 0$, 7.54 km, and 15.08 km. One can see that the intensity profiles are identical except for the successive displacement along the τ axis. Such a self-imaging effect can also be characterized by the cross-correlation coefficient [14]

$$ C = \frac{\int_{-\infty}^{+\infty} I(\tau, z)I(\tau, 0)d\tau}{\left[\int_{-\infty}^{+\infty} I(\tau, z)d\tau \int_{-\infty}^{+\infty} I(\tau, 0)d\tau\right]^{1/2}}, \qquad (10) $$

where $I(\tau, z)$ and $I(\tau, 0)$ are the instantaneous and initial intensity distributions of the pulse train, respectively. The value of C varies from zero to unity and is equal to unity only if the two intensity wave forms are identical. Figure 2(d) shows the evolution of the cross-correlation coefficient as a function of propagation distance in the accelerating coordinate. The coefficient manifests a periodic variation and reaches its maximum close to unity at $z = mz_T$ ($m = 1, 2, \dots$), confirming the self-imaging of the Airy pulse train. Unlike the traditional Talbot effect, here the intensity profiles at the half integer multiplies of Airy-Talbot distance are different from the initial one. The blue dashed curve in Fig. 2(e) denotes the normalized intensity envelope at $z = 3.77$ km, which is distorted by comparing with that at $z = 0$. The reason stems from a phase shift π between adjacent Airy pulses at the location. Additionally, the factor $c_n \exp(-in|\beta_2|Tz/2t_0^3)$ in Eq. (6) is equal to c_n if n is even and $-c_n$ if n is odd. Thus the initial intensity profile has to be reshaped due to the interference between the Airy pulses. The red solid curve in Fig. 2(e) denotes the initial normalized intensity profile with the redefined coefficients $c'_n = (-1)^n c_n$, whose shape is the same with that at $z = 3.77$ km in Fig. 2(a). The particular phenomenon is called the dual Airy-Talbot effect [41].

Additionally, as we choose $c_n = 1$ if n is even and $c_n = i$ if n is odd, the phase shifts between the adjacent Airy pulses become $\pi/2$ at $z = z_T$ and $-\pi/2$ at $z = z_T/2$. Despite that the amplitude $A(\tau, z)$ at $z = z_T$ is conjugate with that at $z = z_T/2$,

the intensity profiles are identical and the dual Airy-Talbot effect disappears. The temporal evolution of the Airy pulse train is shown in Fig. 3(a). Figure 3(b) depicts the normalized intensity profiles at $z = 0$, 3.77 and 7.54 km, indicated by red dashed lines in Fig. 3(a). Unlike the above situation, the intensity profiles at $z = z_T/2$ and $z = z_T$ are identical, which agrees fairly with the theoretical analysis. The variation of the cross-correlation coefficient along the accelerating coordinate is shown in Fig. 3(c), which exhibits periodic oscillation and reaches $C = 1$ at the integer multiples of half Airy-Talbot distance. The same results can also be obtained by choosing $c_n = 1$ as n is even and $c_n = -i$ as n is odd.

Next we investigate the influence of the time interval and main-lobe width of the Airy pulses. For a fixed main-lobe width $t_0 = 10$ ps, the Airy-Talbot distance decreases as the time interval increases, as shown in Figs. 4(a)–4(d). The blue stars in Fig. 4(e) represent the numerical results of acceleration for different T, which are almost identical. The data coincide well with the theoretical analysis for $d^2\tau/dz^2 = \beta_2^2/2t_0^3 = 0.2$ ps/km^2, as plotted with the red line in Fig. 4(e). The blue stars in Fig. 4(f) denote the numerical results of Airy-Talbot distance with respect to T, which are extracted from the cross-correlation coefficients. The results also agree well with the theoretical analysis. The Airy-Talbot effects for different main-lobe widths of the Airy pulses as $T = 83.33$ ps are shown in Figs. 5(a)–5(d). Both the theoretical and numerical data of the acceleration are shown in Fig. 5(e). Figure 5(f) plots the theoretical and numerical results of the Airy-Talbot distance as a function of t_0. It is clearly apparent that the Airy-Talbot distance relates both to the main-lobe width t_0 and time interval T of the Airy pulses, while the acceleration of self-imaging only depends on t_0.

As the input Airy pulse train is modulated by a linearly varying phase, we have

$$ A(\tau, 0) = \sum_{n \in \mathbb{Z}} c_n \text{Ai}\left(\frac{\tau}{t_0} - n\frac{T}{t_0}\right) \exp\left[a\left(\frac{\tau}{t_0} - n\frac{T}{t_0}\right)\right] $$

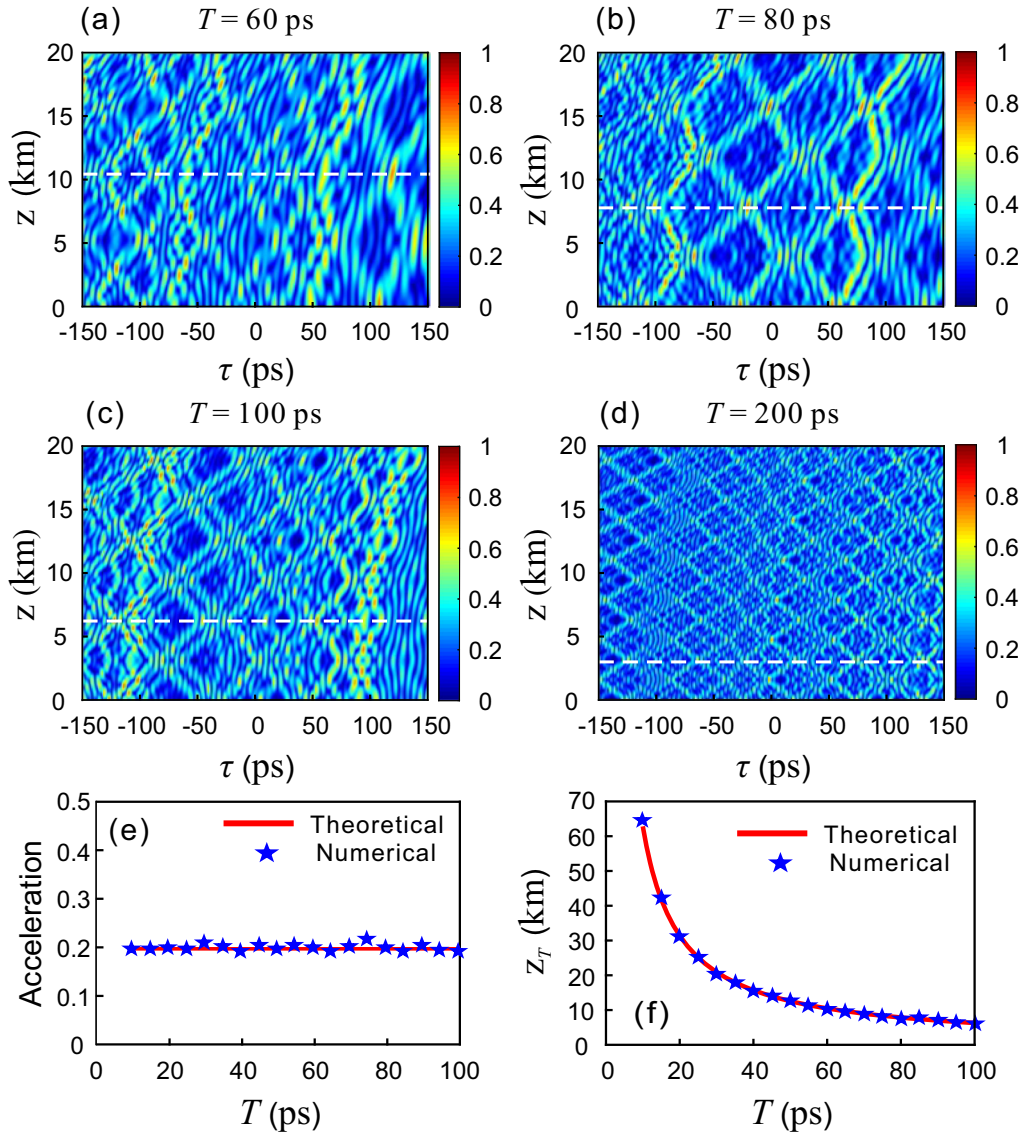$$ \times \exp\left(i\alpha\frac{\tau}{t_0}\right), \qquad (11) $$

FIG. 4. (a)–(d) Temporal evolutions of the wave train vs the time interval T of the Airy pulses; the white dashed lines denote the corresponding Airy-Talbot distances. (e) Theoretical (red line) and numerical (blue stars) results of acceleration vs T. (f) Theoretical and numerical results of Airy-Talbot distance vs T. Other parameters are the same as in Fig. 2(a).

where α stands for the modulation coefficient of the linear phase. In this situation, Eq. (6) becomes

$$I(\tau, z) = \left| \sum_{n \in \mathbb{Z}} c_n \mathrm{Ai}\left(\frac{\tau}{t_0} - \frac{\beta_2{}^2 z^2}{4t_0{}^4} - \alpha \frac{|\beta_2| z}{t_0{}^2} - n\frac{T}{t_0} + ia\frac{|\beta_2|}{t_0{}^2}z \right) \right.$$

$$\times \exp\left(-i\frac{|\beta_2| z}{2t_0{}^3}nT \right)$$

$$\left. \times \exp\left[a\left(\frac{\tau}{t_0} - n\frac{T}{t_0} - \alpha\frac{|\beta_2|}{t_0{}^2}z - \frac{\beta_2{}^2}{2t_0{}^4}z^2 \right) \right] \right|^2. \quad (12)$$

Then the trajectory of self-imaging for $n = 0$ is given by

$$\tau = \frac{\beta_2{}^2}{4t_0{}^3}z^2 + \alpha\frac{|\beta_2|}{t_0}z. \quad (13)$$

The corresponding Newtonian equations read

$$\frac{d^2\tau}{dz^2} = \frac{\beta_2{}^2}{2t_0{}^3} = g,$$

$$\frac{d\tau}{dz} = \alpha\frac{|\beta_2|}{t_0} + \frac{\beta_2{}^2}{2t_0{}^3}z. \quad (14)$$

According to Eqs. (13) and (14), the trajectory and velocity of self-imaging can be manipulated by varying the coefficient α. As $\alpha < 0$, the self-imaging of the Airy pulse train decelerates initially until it stalls at $z = -2\alpha t_0{}^2/|\beta_2|$. Then the self-imaging accelerates along the τ axis, and the transverse displacement is reduced with respect to that of $\alpha = 0$. On the other hand, the transverse shift of the self-imaging will be enhanced as $\alpha > 0$. Figure 6(a) shows the temporal evolution of the pulse train with $\alpha = -1$, where the other parameters are the same as in Fig. 2(a). The wave train repeats itself, shifted along the trajectory $\tau = -2z + 0.1z^2$ for $n = 0$ and
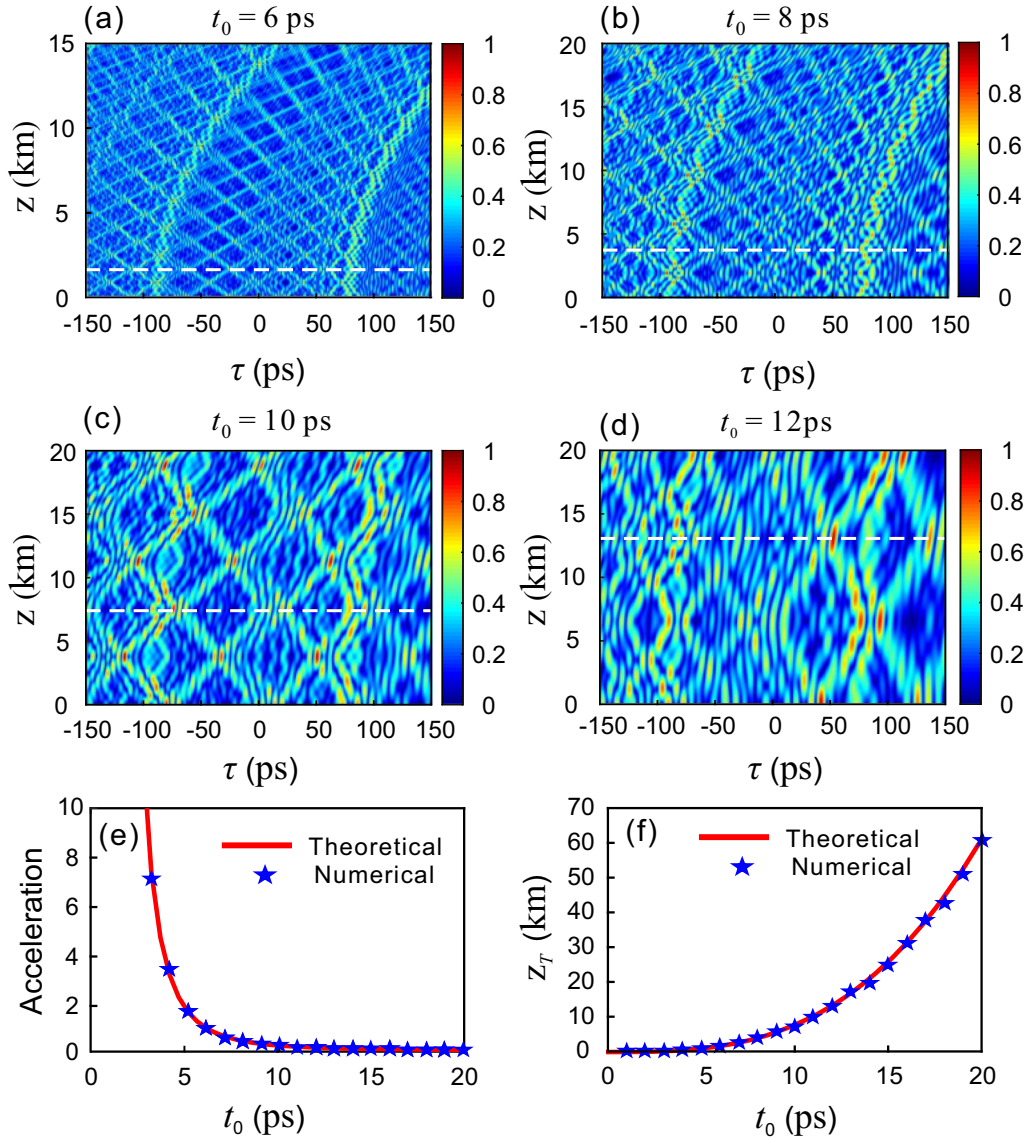
FIG. 5. (a)–(d) Temporal evolutions of the wave train vs the main-lobe width t_0 of the Airy pulses. (e) Theoretical (red curve) and numerical (blue stars) results of acceleration vs t_0. (f) Theoretical and numerical results of Airy-Talbot distance vs t_0. Other parameters are the same as in Fig. 2(a).

reaches its apogee at $z = 10$ km, as plotted with the red dashed curve in Fig. 6(a). The corresponding self-imaging trajectory in the accelerating coordinates is a straight line with a slope of -2, indicated by the red line in Fig. 6(b). In addition, the Airy-Talbot effect as $\alpha = 1$ in the $\tau - z$ plane and in the accelerating coordinates are shown in Figs. 6(c) and 6(d), respectively. The input wave train is self-imaged with the enhanced displacement along the τ axis. The slope of the self-imaging trajectory in the accelerating coordinates is opposite to that of $\alpha = -1$. The solid curves in Fig. 6(e) denote the theoretical self-imaging trajectories for different modulation coefficients of the linear phase. As one can clearly see, for $\alpha = -2$, the decelerate distance is increased and the transverse displacement is further reduced with respect to that of $\alpha = -1$. On the other side, the transverse displacement is further enhanced as $\alpha = 2$. The corresponding results in the accelerating coordinates are shown in Fig. 6(f). The dots in

Figs. 6(e) and 6(f) represent the numerical results of self-imaging positions associated with these cases, which agree well with the theoretical analysis.

B. Airy-Talbot effect in the presence of TOD

In this section, we shall study the influence of TOD on the Airy-Talbot effect. It has been reported that the Airy pulse will exhibit the inversion and tight focusing under the action of positive TOD [30]. By comparing with the case with only GVD in the fiber, the Airy pulse can propagate a longer distance with less dispersion distortion in the presence of negative TOD [31]. We consider the self-imaging for a train of Airy pulses propagating in optical fibers with anomalous GVD and negative TOD. From Eq. (4), the GVD and TOD will bring about distinct phase factors to every Airy pulses, which are dependent on the propagation distance.
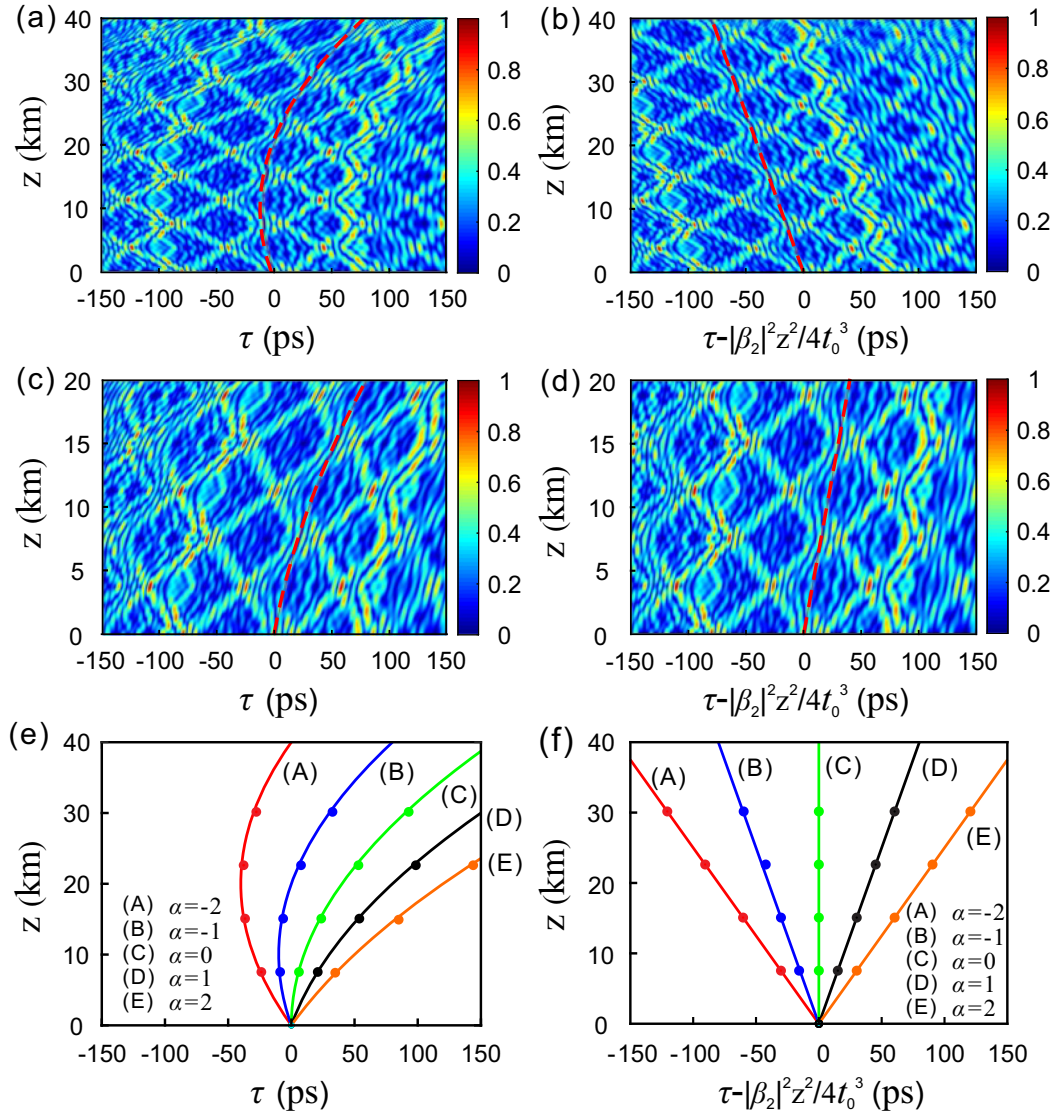
FIG. 6. Temporal evolutions of the Airy pulse train with (a),(b) $\alpha = -1$ and (c),(d) $\alpha = 1$ in the τ-z plane and in the accelerating coordinates, respectively. (e) Numerical self-imaging positions (dots) and theoretical self-imaging trajectories (curves) for different α in the τ-z plane. (f) The corresponding results in the accelerating coordinates. The curves (A)–(E) in (e) and (f) were obtained for $\alpha = -2, -1, 0, 1$, and 2, respectively. Other parameters are the same as in Fig. 2(a).

Analogously, the incident field can recur as the propagation distance L satisfies the condition

$$\frac{1}{\theta^2}\left[\left(-\frac{|\beta_2|L}{2t_0{}^3}T\right) + \left(\frac{b\beta_2{}^2L^2}{2t_0{}^5}T\right)\right] = 2m\pi, \qquad (15)$$

where m is an integer. In particular, Eq. (15) can be satisfied if we set

$$\frac{|\beta_2|L}{2\theta^2t_0{}^3}T = 2k_1\pi,$$

$$-\frac{b\beta_2{}^2L^2}{2\theta^2t_0{}^5}T = 2k_2\pi, \qquad (16)$$

where k_1, k_2 are nonzero integers. Unlike the situations with GVD only, the image at L is temporally expanded with a magnification factor $(1 + |\beta_3|L/2t_0{}^3)^{1/3}$ compared to the input one at $z = 0$, and the corresponding self-imaging trajectory for

$n = 0$ in the τ-z plane is

$$\tau = \frac{\beta_2{}^2z^2}{4t_0(t_0{}^2 - b|\beta_2|z)}. \qquad (17)$$

The analysis can be verified by implementing numerical simulations. Figure 7(a) shows the temporal evolution of a train of Airy pulses under the actions of GVD and TOD simultaneously. In the simulation, the parameters are given as $t_0 = 10\,\mathrm{ps}$, $T = 2\pi \times 10\,\mathrm{ps}$, $\beta_2 = -1\,\mathrm{ps}^2/\mathrm{km}$, and $\beta_3 = -0.8\,\mathrm{ps}^3/\mathrm{km}$. The self-imaging distance can be obtained through Eq. (16). For $k_1 = 3$ and $k_2 = 2$, $L = 1.67 \times 10^3\,\mathrm{km}$. For $k_1 = 2$ and $k_2 = 8$, $L = 1 \times 10^4\,\mathrm{km}$. The two locations of self-imaging are marked by the white dotted lines in Fig. 7(a). The red dashed curve in Fig. 7(a) denotes the trajectory described by Eq. (17). Figure 7(b) shows the normalized intensity profiles at $z = 0$, $1.67 \times 10^3\,\mathrm{km}$, and $1 \times 10^4\,\mathrm{km}$. It
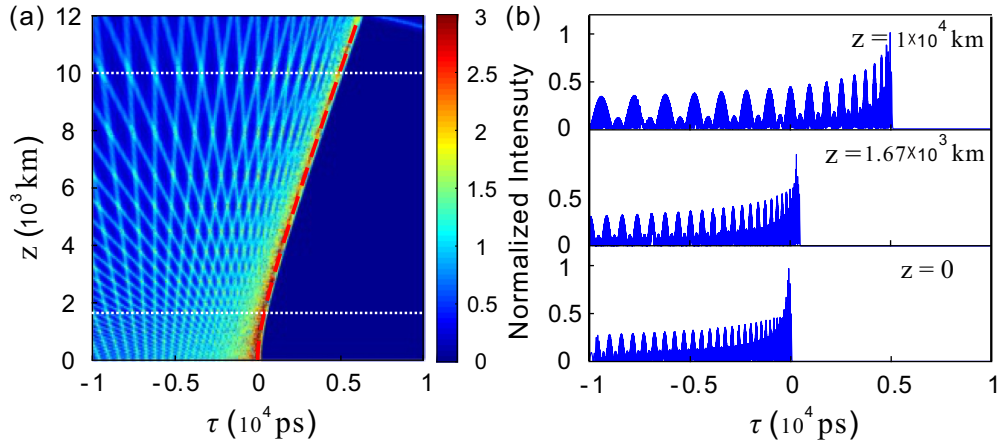
FIG. 7. (a) Temporal evolution of the Airy pulse train under the actions of GVD and TOD simultaneously. The white dotted lines represent the two self-imaging positions and the red dashed curve denotes the self-imaging trajectory for $n = 0$. (b) Normalized intensity profiles at $z = 0$, 1.67×10^3 km, and 1×10^4 km. Parameters are $t_0 = 10$ ps, $T = 2\pi \times 10$ ps, $\beta_2 = -1$ ps^2/km, and $\beta_3 = -0.8$ ps^3/km.

is found that the intensity profiles have similar shapes. As the distance increases, the profile is magnified proportionally in the time dimension.

C. Finite-energy Airy-Talbot effect

It has been revealed that the temporal Airy-Talbot effect can be observed for a wave train formed by the superposition
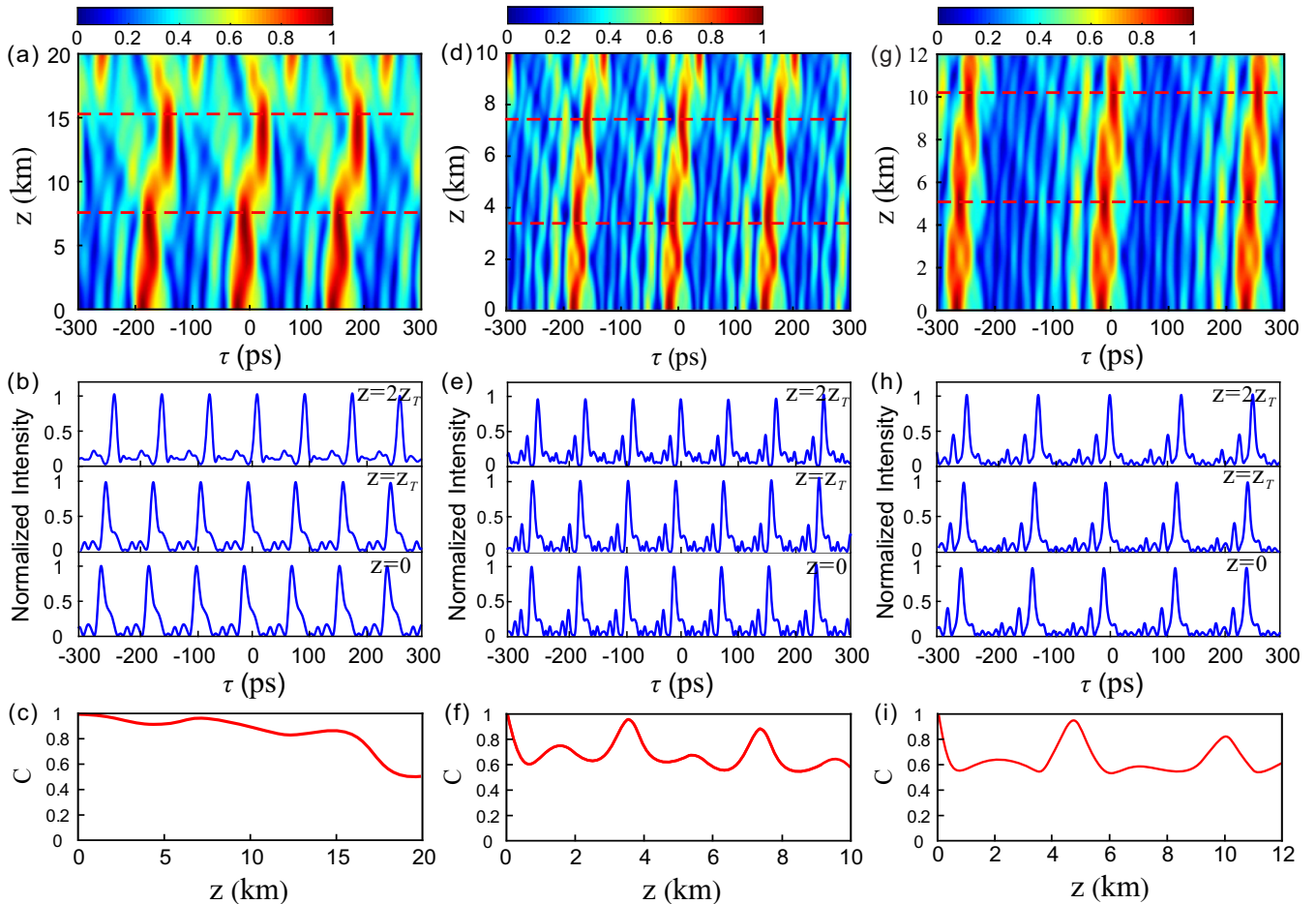

FIG. 8. Temporal evolutions of Airy pulse trains composed by the truncated Airy pulses with $c_n = 1$ for all components (the top row). The corresponding normalized intensity profiles at $z = 0$, z_T, and $2z_T$ (the middle row) and the variations of cross-correlation coefficients along the accelerating coordinates (the bottom row). Other parameters are the same as in Fig. 2(a) except for $t_0 = 8$ ps in (d)–(f) and $T = 125$ ps in (g)–(i). $a = 0.1$.

of ideal Airy pulses. However, the ideal Airy pulses possess limitless time duration and infinite energy. In practice, we have to truncate the pulses so as to make them have finite energy. As a result, similar to truncated Airy beams in space, the truncated Airy pulses will experience dispersion and the acceleration feature never maintains after a certain distance. Beyond the accelerating range, which is comparable to the dispersion length [37], the intensity profile of the pulses becomes from Airy-like to Gaussian-like [22]. Here, we choose the truncation factor $a = 0.1$ and $c_n = 1$ for all Airy pulse components, and the other parameters remain unchanged. The temporal evolution of the incident field is illustrated in Fig. 8(a), where the self-imaging effect disappears very quickly. Figure 8(b) shows the normalized intensity profiles at $z = 0$, 7.54 km, and 15.08 km; the wave train is getting closer to a sequence of Gaussian-like pulses as the propagation distance increases. And the cross-correlation coefficient decreases as z increases; see the red curve in Fig. 8(c). The reason lies in the fact that the Airy-Talbot distance is beyond the self-accelerating range of the Airy pulses. Therefore, for finite-energy Airy pulses, one has to shorten the Airy-Talbot distance to make sure that the accelerating range is long enough for the formation of self-imaging. According to Eq. (9), the Airy-Talbot distance can be decreased by decreasing the main-lobe width t_0 or enlarging the time interval T of the Airy pulses. For instance, we decrease the main-lobe width to $t_0 = 8$ ps by comparing with that in Fig. 8(a), then the Airy-Talbot distance becomes $z_T = 3.86$ km. As illustrated in Fig. 8(d), the accelerating self-imaging phenomenon can be observed. The red dashed lines in Fig. 8(d) denote the two self-imaging positions of $z = 3.86$ km and $z = 7.72$ km, the intensity profiles at which are the same with that at $z = 0$, as shown in Fig. 8(e). Figure 8(f) shows the evolution of the cross-correlation coefficient along the accelerating coordinate, which varies nearly periodically and reaches its maximum near unity at the self-imaging positions. It clearly validates the Airy-Talbot effect. In addition, the Airy-Talbot effect can also be observed by enlarging the time interval T of the pulses. The temporal evolution of the Airy pulse train with $T = 125$ ps in the τ-z plane is shown in Fig. 8(g), where the other parameters are the same as in Fig. 8(a). The red dashed lines in Fig. 8(g) denote the first and second self-imaging locations at $z_T = 5.03$ and 10.06 km, the corresponding intensity profiles at which are identical to the input one at $z = 0$, as depicted in Fig. 8(h). The periodic variation of the cross-correlation coefficient is shown in Fig. 8(i), which also validates the self-imaging effect of the finite-energy Airy pulse train.

IV. CONCLUSIONS

In conclusion, we have theoretically demonstrated the temporal accelerating self-imaging effect for a train of Airy pulses. Due to the self-acceleration of the Airy pulses, the self-imaging of the incident field is shifted along the parabolic trajectories in the τ-z plane. The self-imaging distance can be manipulated by varying the main-lobe width and the time interval of the Airy pulses, where the acceleration itself is determined by the pulse main-lobe width. Unlike the traditional Talbot effect, the incident field needs not be periodic, but instead can have an almost arbitrary profile as a superposition of Airy pulses with different intensities and phases. In addition, the trajectory of self-imaging can be modified by imposing a linearly varying phase on the input pulse train. Furthermore, the pulse train exhibits the temporally magnified self-imaging effect under the action of TOD. For ideal Airy pulses, the self-imaging maintains indefinitely. For the truncated Airy pulses, the self-imaging can be observed only in a limited distance. Our study paves a promising way to control the self-imaging of optical pulses and may find applications in information processing and transmission in optical fibers.

APPENDIX

In this Appendix, we briefly describe the simulations of the Airy pulse train propagating in optical fibers by using the split-step Fourier transform method. Equation (1) can be written as

$$i\frac{\partial A}{\partial z} = (\hat{D} + \hat{N})A, \tag{A1}$$

where the dispersion operator $\hat{D}$ and nonlinear operator $\hat{N}$ are given by

$$\hat{D} = -\frac{1}{2}\beta_2\frac{\partial^2}{\partial\tau^2} + \frac{1}{6}\beta_3\frac{\partial^3}{\partial\tau^3}, \quad \hat{N} = 0. \tag{A2}$$

Inspired by the split-step Fourier transform method, we have

$$A(\tau, z + \Delta z) = A(\tau, z)\exp[i(\hat{D} + \hat{N})\Delta z]. \tag{A3}$$

In our model, the nonlinear operator is absent, thus the optical field distribution of the wave train after the propagation distance h can be described as

$$A(\tau, z + h) = \mathscr{F}^{-1}\left\{\mathscr{F}[A(\tau, z)]\exp\left(i\frac{\beta_2 h}{2}\omega^2 + i\frac{\beta_3 h}{6}\omega^2\right)\right\}, \tag{A4}$$

where $\mathscr{F}$ and $\mathscr{F}^{-1}$ represent the Fourier transform and inverse Fourier transform, respectively. In the calculations, we choose $h = 100$ m, which is sufficient to ensure the accuracy of simulation results.

[1] H. F. Talbot, Philos. Mag. **9**, 401 (1836).

[2] L. Deng, E. W. Hagley, J. Denschlag, J. E. Simsarian, M. Edwards, C. W. Clark, K. Helmerson, S. L. Rolston, and W. D. Phillips, Phys. Rev. Lett. **83**, 5407 (1999).

[3] W. Zhang, C. Zhao, J. Wang, and J. Zhang, Opt. Express. **17**, 19757 (2009).

[4] W. Zhang, X. Huang, and Z. Lu, Opt. Express **19**, 15297 (2011).

[5] R. Iwanow, D. A. May-Arrioja, D. N. Christodoulides, G. I. Stegeman, Y. Min, and W. Sohler, Phys. Rev. Lett. **95**, 053902 (2005).

[6] S. Wang, B. Wang, S. Ke, C. Qin, K. Wang, H. Long, and P. Lu, Opt. Quantum Electron. **49**, 389 (2017).

[7] H. Ramezani, D. N. Christodoulides, V. Kovanis, I. Vitebskiy, and T. Kottos, Phys. Rev. Lett. **109**, 033902 (2012).

[8] Y. Zhang, J. Wen, S. N. Zhu, and M. Xiao, Phys. Rev. Lett. **104**, 183901 (2010).

[9] Y. Zhang, M. R. Belic, H. Zheng, H. Chen, C. Li, J. Song, and Y. Zhang, Phys. Rev. E **89**, 032902 (2014).

[10] X. B. Song, H. B. Wang, J. Xiong, K. Wang, X. Zhang, K. H. Luo, and L. A. Wu, Phys. Rev. Lett. **107**, 033902 (2011).

[11] F. Pfeiffer, M. Bech, O. Bunk, P. Kraft, E. F. Eikenberry, C. Brönnimann, C. Grunzweig, and C. David, Nat. Mater. **7**, 134 (2008).

[12] G. P. Agrawal, *Nonlinear Fiber Optics* (Academic, New York, 2013).

[13] T. Jannson and J. Jannson, J. Opt. Soc. Am. **71**, 1373 (1981).

[14] J. Azana and M. A. Muriel, Appl. Opt. **38**, 6700 (1999).

[15] R. Maram, J. Van Howe, M. Li, and J. Azaña, Nat. Commun. **5**, 5163 (2014).

[16] S. Wang, C. Qin, B. Wang, and P. Lu, Opt. Express **26**, 19235 (2018).

[17] J. Azaña and M. A. Muriel, IEEE J. Sel. Topics Quantum Electron. **7**, 728 (2001).

[18] J. Wen, Y. Zhang, and M. Xiao, Adv. Opt. Photon. **5**, 83 (2013).

[19] J. Turunen, A. Vasara, and A. T. Friberg, J. Opt. Soc. Am. A **8**, 282 (1991).

[20] T. Saastamoinen, J. Tervo, P. Vahimaa, and J. Turunen, J. Opt. Soc. Am. A **21**, 1424 (2004).

[21] Y. Lumer, L. Drori, Y. Hazan, and M. Segev, Phys. Rev. Lett. **115**, 013901 (2015).

[22] G. A. Siviloglou and D. N. Christodoulides, Opt. Lett. **32**, 979 (2007).

[23] G. A. Siviloglou, J. Broky, A. Dogariu, and D. N. Christodoulides, Phys. Rev. Lett. **99**, 213901 (2007).

[24] M. V. Berry and N. L. Balazs, Am. J. Phys. **47**, 264 (1979).

[25] N. K. Efremidis and D. N. Christodoulides, Opt. Lett. **35**, 4045 (2010).

[26] I. Kaminer, R. Bekenstein, J. Nemirovsky, and M. Segev, Phys. Rev. Lett. **108**, 163901 (2012).

[27] J. Broky, G. A. Siviloglou, A. Dogariu, and D. N. Christodoulides, Opt. Express **16**, 12880 (2008).

[28] C. Chang, H. P. Sardesai, and A. M. Weiner, Opt. Lett. **23**, 283 (2015).

[29] I. Kaminer, Y. Lumer, M. Segev, and D. N. Christodoulides, Opt. Express **19**, 23132 (2011).

[30] R. Driben, Y. Hu, Z. Chen, B. A. Malomed, and R. Morandotti, Opt. Lett. **38**, 2499 (2013).

[31] I. M. Besieris and A. M. Shaarawi, Phys. Rev. E **78**, 046605 (2008).

[32] L. Zhang, K. Liu, H. Zhong, Y. Li, and D. Fan, Opt. Express **23**, 2566 (2015).

[33] T. Han, H. Chen, C. Qin, W. Li, B. Wang, and P. Lu, Phys. Rev. A **97**, 063815 (2018).

[34] Y. Fattal, A. Rudnick, and D. M. Marom, Opt. Express **19**, 17298 (2011).

[35] S. Wang, D. Fan, X. Bai, and X. Zeng, Phys. Rev. A **89**, 023802 (2014).

[36] C. Ament, P. Polynkin, and J. V. Moloney, Phys. Rev. Lett. **107**, 243901 (2011).

[37] L. Zhang, H. Zhong, Y. Li, and D. Fan, Opt. Express **22**, 22598 (2014).

[38] G. A. Siviloglou, J. Broky, A. Dogariu, and D. N. Christodoulides, Opt. Lett. **33**, 207 (2008).

[39] C. Qin, F. Zhou, Y. Peng, D. Sounas, X. Zhu, B. Wang, J. Dong, X. Zhang, A. Alu, and P. Lu, Phys. Rev. Lett. **120**, 133901 (2018).

[40] C. Z. Qin, L. Q. Yuan, B. Wang, S. H. Fan, and P. X. Lu, Phys. Rev. A **97**, 063838 (2018).

[41] Y. Zhang, H. Zhong, M. Belic, X. Liu, W. Zhong, and M. Xiao, Opt. Lett. **40**, 5742 (2015).